

Numerical study of double-pulse laser ablation of Al

G. D. Förster* and Laurent J. Lewis†

Département de Physique et Regroupement Québécois sur les Matériaux de Pointe (RQMP), Université de Montréal, C.P. 6128, succursale Centre-ville Montréal, H3C 3J7 Québec, Canada



(Received 10 November 2017; revised manuscript received 1 February 2018; published 1 June 2018)

The effect of double laser pulses (DPs) on the ablation process in solids is studied using a hybrid two-temperature model combining a continuum description of the conduction band electrons with a classical molecular dynamics (MD) approach for the ions. The study is concerned with double pulses with delays in the range of 0–50 ps and absorbed laser fluences of 0.5, 1.0, and 1.5 J/m² [i.e., 1–3 times the ablation threshold for single-pulse ablation (SP)], taking Al as a generic example of simple metals. A detailed analysis, including the assessment of thermodynamic pathways and cavitation rates, leads to a comprehensive picture of the mechanisms active during the different stages of the ablation process initiated by DPs. This study provides an explanation for several phenomena observed in DP ablation experiments. In particular, with respect to SP ablation, crater depths are reduced, which can be explained by the compensation of the rarefaction wave from the first laser pulse with the compression wave from the second pulse, or, at higher fluences and larger delays, by the fact that the target surface is shielded with matter ablated by the first laser pulse. Also, we discuss how smoother surface structures obtained using DPs may be related to features found in the simulations—viz., reduced mechanical strain and peak lattice temperatures. Finally, vaporization appears to be enhanced in DP ablation, which may improve the resolution of emission spectra.

DOI: [10.1103/PhysRevB.97.224301](https://doi.org/10.1103/PhysRevB.97.224301)

I. INTRODUCTION

The essence of laser ablation is the removal of matter from the surface of a target via intense laser irradiation. In metals, electrons from the conduction band are heated by the laser. The hot electron gas subsequently excites phonons in the lattice and equilibrates on a picosecond timescale [1]. Depending on fluence, different portions of the target melt, are vaporized or even form a plasma. This process generates a high-pressure region near the surface which subsequently propagates as compression waves towards the surface and into the target. The reflection of the compression wave at the surface yields a rarefaction wave that travels behind the compression wave into the bulk. If intense enough, the rarefaction wave induces failure near the surface, causing large pieces of matter to detach in a process known as spallation [2–4]. As the material expands and cools, regions of the target enter thermodynamically metastable states that may decompose rapidly into a plume of clusters of different sizes (phase explosion) [5]. In this work, we investigate how this process is modified if a second laser pulse strikes the target at different time delays after the first pulse.

During the ablation process, a plume of ions, neutral atoms, and larger fragments is generated. Laser ablation can thus be used for the fabrication of nanoparticles (NPs) and film growth [6–8]. For applications, it is essential to control the composition, crystallinity, size, and shape of the particles [9]. In the case of ablation with single ultrashort pulses (SPs), the influence

of target material [10,11], pulse duration [12], wavelength [13,14], and fluence [11,12,15,16] on the distribution in size of the synthesized NPs [17,18] is relatively well understood, but control over the ablation process is somewhat limited. The use of long and double pulses (DPs) has been discussed as a means to influence particle properties [19–21].

Other applications may also benefit from the use of DPs. For example, ultrashort laser pulses are a valuable tool for micromachining thanks to their high processing speed, precision, and low sample heating [22]. The influence of target material, fluence, and pulse duration on ablation thresholds and rates has been studied in detail [23–25]. It has been suggested that this technology can be improved by the use of DPs [26]. Finally, laser-induced breakdown spectroscopy (LIBS) is an application of ablation for cheap, fast, and versatile material analysis [27–29]. For many LIBS applications it is desirable that ablation is as little destructive as possible. Therefore, sample heating and the total mass of the ablated material should be kept small, while the spectral resolution and signal intensity is maximized. These objectives can be achieved by DP ablation with a carefully chosen delay [30–33].

In view of this, knowledge of the details of the DP ablation process is important for further developments. Assuming two identical pulses, the most important features of DP ablation on metals as a function of delay may be understood in terms of three regimes [30,34].

Regime I. For DP delays below the electron-phonon equilibration time (0.5–0.9 ps [35]), ablation produces results close to those from SP ablation with twice the fluence [22,30,34]. In this regime, ablation processes are independent of delay [36]. It seems therefore that only the total amount of energy deposited is important, irrespective of its distribution in time [30]. This

*daniel.forster@umontreal.ca

†laurent.lewis@umontreal.ca

is however not the case for semiconductors, where DPs affect the ablation process significantly in this delay regime [37].

Regime II. For DP delays up to ten times the electron-phonon equilibration time, it has been demonstrated that cleaner, smoother structures can be produced by optimizing laser pulse shapes in the case of metals [38] as well as dielectrics [39]. Additionally, a reduction in the area affected by the laser has been experimentally observed [40] and reproduced in numerical studies [41,42]. Experimental studies show that the ablation depth and yield may approach values similar to, or even smaller than, those obtained with SPs [20,36,43,44]. These findings could be reproduced for Cu [45,46] and Al [47] using a hydrodynamic model, and for Al using atomic-level simulations [47–49]. The reduction of the ablation depth has been explained by the fact that the rarefaction wave from the first pulse is compensated by the compression wave from the second pulse [45,46]. However, other experimental studies show an increase in ablation efficiency for DPs with delays on the order of 10 ps in the case of Cu [50], steel [51], and Si [37]. Other atomic-level simulations of Al show that thin-film oscillations can be enhanced or attenuated depending on DP delay and the ratio of the film thickness to the speed of sound [52].

The number of single atoms and ions in the plume increases with delay at the expense of larger fragments, which is explained by the decomposition of NPs by the second pulse [19,20,53]. Therefore, even though DPs reduce the overall ablation yield, the number of monomers in the ablation plume increases. Debris deposited around the ablation crater declines in granularity and spreads over larger areas with increasing delay. This is indicative of the existence of an inverse correlation between fragment size and ejection velocity [54]. The energy of the second laser pulse is mainly absorbed in the front portion of the ablation plume, leading to further excitation there [55]. Luminosity is enhanced by increasing the number of atoms in an excited state due to plasma reheating [20,56].

Regime III. At DP delays exceeding ten times the electron-phonon equilibration time, the ablated material from the first pulse shields the remaining target from further ablation [30,43,54], thus reducing the crater depth further [20,30]. This regime is particularly interesting for LIBS because of high plasma luminosity (an order of magnitude increase with respect to SP ablation), good pulse-to-pulse reproducibility, and spherical plasma shapes, while the target surface remains unaffected from the second pulse due to the shielding effect [30].

Eventually, at even larger delays the plasma again becomes transparent for the second pulse and the two pulses act independently [34]. The characteristic double-pulse delays that define these regimes do not depend on either fluence or target material [30]. However, the variation of ablation rate and depth with delay becomes less pronounced with increasing laser fluence [36].

DP ablation is a relatively new method and has not yet been fully explored [44]. Several experimental studies have provided information on the outcome of ablation with regards to plume emission, ablation yield, crater, NP formation, etc. However, the underlying mechanisms are less clear than in the SP case [22,36,43,53]. The present study is concerned with different features of DP ablation, such as reduced ablation

depth, weaker pressure waves, and enhanced vaporization, and explains them on the grounds of data gathered from atomic-level simulations. Ultimately, such knowledge could help identify promising conditions for ultrashort DP ablation with regards to some of the applications mentioned earlier. These observations, together with our previous work in this area, motivated the present study.

In view of this, we investigated the effect of DP delay (in the range of 0–50 ps) on the mechanisms active during the different stages of ablation, making use in particular of the thermodynamic pathway analysis of the ablation process introduced by Perez *et al.* [57,58]. The present study focuses on Al as a generic example and a widely investigated material for laser ablation [30,47,48,54,59–62]. In contrast to ablation with ultrashort SPs, the laser interacts with material in the extreme conditions induced by the first pulse. We employ a hybrid two-temperature model (TTM) consisting of a heat equation for the electrons solved in a 3D finite-difference (FD) scheme, instead of the commonly used 1D description [36,47–49], and classical molecular dynamics (MD), which allows for a realistic description of metallic interactions. The MD part is based on the embedded-atom-method (EAM) potential for Al by Zope and Mishin [63]. The electronic model follows the description of the thermal conductivity of electrons by Inogamov and Petrov [1] and the calculations of the electronic heat capacity and the electron-phonon coupling by Lin and coworkers [64]. Section II provides the details of this model.

Our results are presented in Sec. III. In particular, our simulations reveal the nature of the precise mechanisms leading to the decrease of ablation depth observed in DP ablation. First, at DP delays on the order of 10 ps, the rarefaction wave from the first pulse is very much compensated by the compression wave generated by the second pulse. Second, at fluences of several times the ablation threshold and DP delays in excess of 10 ps, much of the energy of the second pulse is absorbed by the material spalled from the first pulse. Both of these mechanisms reduce the strength of the rarefaction wave, which would otherwise drive the material into a thermodynamically metastable state, increasing the likelihood of phase explosion, the dominant ablation mechanism at the fluences studied here. In addition, the intensity of the compression wave and peak lattice temperatures are also reduced at DP delays of tens of picoseconds. This decreases strain on the target, explaining smoother ablation craters and reduced microcrack formation. Furthermore, the simulations show that vaporization increases with DP delay: the first pulse causes the top portion of the target to melt and, at higher fluence, to undergo phase explosion. After some tens of picoseconds, this creates a hot, foamy structure with a large internal surface area. The second pulse interacts with this structure and increases vaporization by a large amount. As emission spectra depend on the number of monomers at high temperature, this explains the enhanced spectral resolution found in DP ablation. The overall picture is briefly reviewed in Sec. IV, which also provides an outlook on future work.

II. SIMULATION MODEL

The TTM describes the out-of-equilibrium state of electrons and ionic cores by assigning a temperature to both subsystems

and allowing for energy transfer between the two. Free electrons in the conduction band absorb laser photons and gain energy. They equilibrate very rapidly and transfer the energy to the ionic subsystem.

A. Electronic subsystem

The electronic subsystem is modeled with the diffusion equation [Eq. (1) below] for the electronic temperature T_e , which we solve in a FD scheme (we assume that the laser is incident from the positive z direction). In order to properly account for the material ablated by the first pulse when the second pulse arrives, we use a FD scheme with a 3-dimensional grid of cells. This 3D solution has been used in the large-scale simulations of Ref. [18], where the authors note that such a description is important to account for the large density fluctuations that lead to complex 3D heat flows. However, we find, after analyzing our simulations, that at least for our system size and laser fluences, this 3D approach does not improve significantly the accuracy of the calculation as electronic heat lateral gradients remain limited even as the second laser pulse interacts with the surface of the target containing important density fluctuations from bubble formation. The FD cells have a volume $V_c = \Delta x \times \Delta y \times \Delta z$, with $\Delta x = \Delta y \approx 0.84$ nm and $\Delta z \approx 0.81$ nm. The diffusion equation is

$$C_e(T_e) \frac{\partial T_e}{\partial t} = \nabla [K_e(T_e, T_i) \nabla T_e] - \Gamma(T_e)(T_e - T_i) + Q(\vec{r}, t). \quad (1)$$

The electronic heat capacity $C_e(T_e)$ and the electron-phonon coupling parameter $\Gamma(T_e)$ are taken from Ref. [64]. Moreover, we use the formulation for the electronic heat conductivity $K_e(T_e, T_i)$ proposed by Inogamov and Petrov that is valid over a wide range of electronic temperatures up to the Fermi temperature [1]. The lattice or ionic temperature T_i is calculated within the MD description, individually for each FD cell. We take the two pulses to be identical and delayed by t_D , and thus the laser source term $Q(\vec{r}, t)$ takes the form

$$Q(\vec{r}, t) = \frac{F \times \rho(\vec{r}, t)}{\sqrt{2\pi} d \rho_0 \alpha} \left\{ \exp \left[-\frac{1}{2} \frac{(t - t_0)^2}{d^2} \right] + \exp \left[-\frac{1}{2} \frac{(t - t_0 - t_D)^2}{d^2} \right] \right\} \times \exp(-\tau), \quad (2)$$

where $t_0 = 2d$, d being the Gaussian width of an individual laser pulse which we set to 200 fs. According to the Beer-Lambert-Bouguer law, the laser intensity decreases exponentially with optical depth,

$$\tau = \frac{\int_{\vec{r} \cdot \vec{e}_z}^{\infty} \rho(\vec{r}, t) dz}{\rho_0 \alpha}, \quad (3)$$

where $\rho(\vec{r})$ designates the density of the material at position \vec{r} and α is the penetration length. Assuming a laser wavelength of 800 nm, $\alpha = 7.53$ Å for Al [65]. The reference density for the penetration length is $\rho_0 = 2700$ kg/m³ for Al in normal conditions. In the following, we examine the effect of DPs with delays t_D of 0, 0.4, 2, 10, and 50 ps, and total absorbed fluences F (i.e., the two pulses combined) of 0.5, 1.0, and 1.5 kJ/m², that is, 1–3 times the ablation threshold for SPs

(0.55 ± 0.05 kJ/m² for the present model [60]). More details on the electronic model can be found in Appendix A.

B. Ionic subsystem

The energy of the electrons heated by the laser is transferred to the ionic subsystem via the following modified equation of motion [66]:

$$m_i \frac{d^2 \vec{r}_i}{dt^2} = \vec{F}_i + \xi m_i \vec{v}_i^T, \quad (4)$$

where \vec{F}_i represents the force acting on atom i of mass m_i at position \vec{r}_i . The thermal velocity \vec{v}_i^T is the velocity of atom i from which the center-of-mass velocity of the atoms in the FD cell to which it belongs has been subtracted. The quantity ξ , finally, is given by

$$\xi = \frac{1}{n} \sum_{k=1}^n \Gamma_k(T_e) V_c [(T_e)_k - T_i] / \sum_{i \text{ in } V_c} m_i (v_i^T)^2 \quad (5)$$

in Ref. [66]. In the above, the first sum runs over the n FD time steps Δt_{FD} that are carried out every MD time step $\Delta t_{\text{MD}} = 2$ fs. The smallest possible value of n can be determined via the von Neumann stability criterion [66]:

$$\Delta t_{\text{FD}} \leq \frac{1}{2} (\Delta x^{-2} + \Delta y^{-2} + \Delta z^{-2})^{-1} C_e / K_e \quad (6)$$

and consequently $n = \lceil \Delta t_{\text{MD}} / \Delta t_{\text{FD}} \rceil$. In practice, we used 300 FD integration steps for every MD integration step, which is about 10% more than required by the stability criterion. The forces \vec{F}_i are derived from the EAM potential for Al by Zope and Mishin [63], of which we have assessed the high-temperature properties in a series of preliminary simulations (see Appendix B).

The target consists of an Al fcc crystal containing 4.9 million atoms arranged in 1000 layers of 35×35 unit cells with the (100) surface exposed to the laser beam which arrives from the $+z$ direction. We employ periodic boundary conditions laterally and open boundaries in the direction of laser incidence, plus a shock-absorbing layer at the bottom [67]. In this layer, forces due to interactions with the atoms above are replaced by $-A \zeta v_z / m$, v_z being the z speed of the atom, A the atomic cross section, and $\zeta = \rho_0 c_0$ the mechanical impedance, where $c_0 = 4.2$ km/s is the speed of sound in the target [60].

In the region beyond this boundary, the ionic subsystem is modeled by a continuum equation similar to that for the electronic system, as found in the original TTM formulation [68]:

$$C_i(T_i) \frac{\partial T_i}{\partial t} = \Gamma(T_e)(T_e - T_i), \quad (7)$$

where $C_i = 2.422$ J m⁻³ K⁻¹ is the volumetric ionic specific heat of Al. In this region heat diffusion is neglected.

The electronic equation is solved on a lattice of 1512 layers containing 17×17 cells each, spanning the entire MD domain plus a slab of 0.6 μm above the initial surface for accommodating the ablation plume and 0.2 μm behind the MD block for a smooth transition to the bulk of the target. Prior to the main simulations, the MD part of the system has

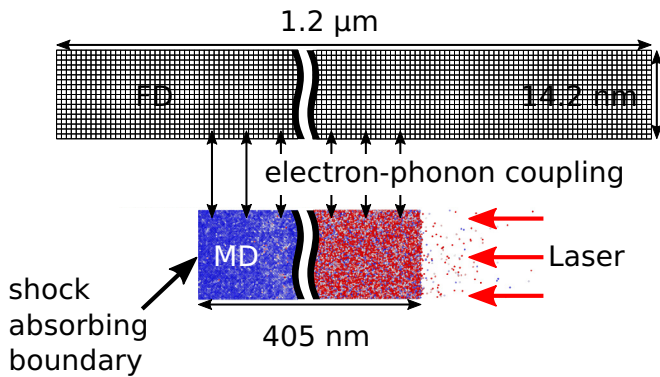


FIG. 1. Schematic of the TTM consisting of the FD scheme for the electronic system and the EAM MD description for the atomic cores. Al atoms are represented by small circles, color-coded according to their centrosymmetry parameter [69]: blue corresponds to a crystalline state and red to a liquid-like state. The system dimensions are $14.2 \times 14.2 \text{ nm}^2$ in the plane perpendicular to laser incidence and $1.2 \mu\text{m}$ parallel to it. Initially, the MD region fills a slab of thickness 405 nm . The space above the target surface is necessary to accommodate the ablated material; the FD region beyond the shock absorbing boundary of the MD section serves as a buffer ensuring a smooth transition to the bulk of the target. Due to the high aspect ratio, the representation of the target is broken up as indicated by the curvy lines.

been relaxed at 300 K and zero pressure over a period of 100 ps using a Berendsen thermostat and barostat. A visualization of this setup is presented in Fig. 1.

C. Limitations of the model

A limitation of the present model is that it considers only *absorbed* laser fluences. The decreasing reflectivity and increasing absorption due to phase and temperature changes induced by the first laser pulse are not considered. The changes of the absorption profile are assessed in Ref. [49]. In addition, the authors propose a method using the Helmholtz wave equation based on an empirical high-frequency dielectric function to overcome this shortcoming [70]. The experimental equivalent of this study would involve a pair of laser pulses with decreasing fluence. In particular, the complex foamy structure found at the target surface when the second laser pulse arrives makes the importance of this effect difficult to estimate. These geometries with large-scale fluctuations in density are another difficulty for atomistic simulations. Voids, droplets, and particles are limited by the size of the simulation cell. In particular, voids easily outgrow the lateral dimensions of the simulated system. This leads to the detachment of entire target layers or “spallation,” which occurs therefore in this type of simulation earlier than in real systems. Our system can accommodate spherical bubbles of 1500 nm^3 . This volume is reached by the largest bubble in our simulations within $40\text{--}120 \text{ ps}$ after the arrival of the first laser pulse, with the exception of ablation at 0.5 kJ/m^2 where bubbles of this size never occur in the case of delays of $0, 10, \text{ and } 50 \text{ ps}$. Quantitative comparisons to experimental results are limited because of the inability of the present EAM potential to reproduce correctly the high-temperature properties of Al, such as the critical

point. This description represents therefore a generic model for the ablation of simple metal targets. As important as this may seem, comparison of the thermodynamic pathways from simulations based on another EAM potential with a much lower critical temperature show remarkable agreement [18]. Finally, the present model is limited to the low-fluence ablation regime due to its failure to account for ionization and plasma effects in the ablation plume.

III. RESULTS

We begin by discussing the evolution in time of the distribution of matter in the target and ablation plume after the absorption of the laser energy. Next, the thermodynamic state in different parts of the system is assessed; in particular, the properties of the pressure wave in the target show an interesting dependence on fluence and DP delay. Finally, we examine the formation of subsurface voids in the target and ablation efficiency.

A. Visual inspection of simulation snapshots

Figure 2 shows the top portion of the target after irradiation with DPs of different delays and fluences, 200 ps after the first laser pulse. The atoms are colored according to their centrosymmetry parameter [69], which measures the departure of an atomic site from the perfect local crystalline environment: atoms colored in blue have a crystalline fcc environment, and atoms in red are associated with the disordered, liquid phase. At low total absorbed fluence, 0.5 kJ/m^2 (close to the ablation threshold), the surface remains essentially intact and no significant pieces of material are removed. Figure 2 shows the final snapshots of the simulations; the time evolution of the atomic positions as well as the evolution of the subsurface voids can be found in the Supplemental Material [72,73], respectively. These animations show that at this lowest fluence

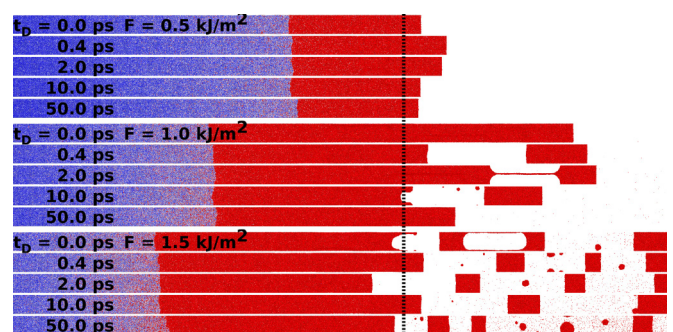


FIG. 2. Snapshots (generated using the OVITO software [71]) of the system for various DP delays and fluences, taken after a simulation time of 200 ps following the first laser pulse. The snapshots show the top portion of the target, extending from -300 to 200 nm with respect to the initial surface (at $z = 0$, indicated by the dotted line) and the full width of 14.2 nm . The atoms are colored according to their centrosymmetry parameter [69], ranging from 0 (blue, crystalline) to 1.5 \AA^2 (red, liquid). The laser is incident from the right. An animation (all values of fluences and delays considered in the present work) with the full time evolution of the target can be found in the Supplemental Material [72].

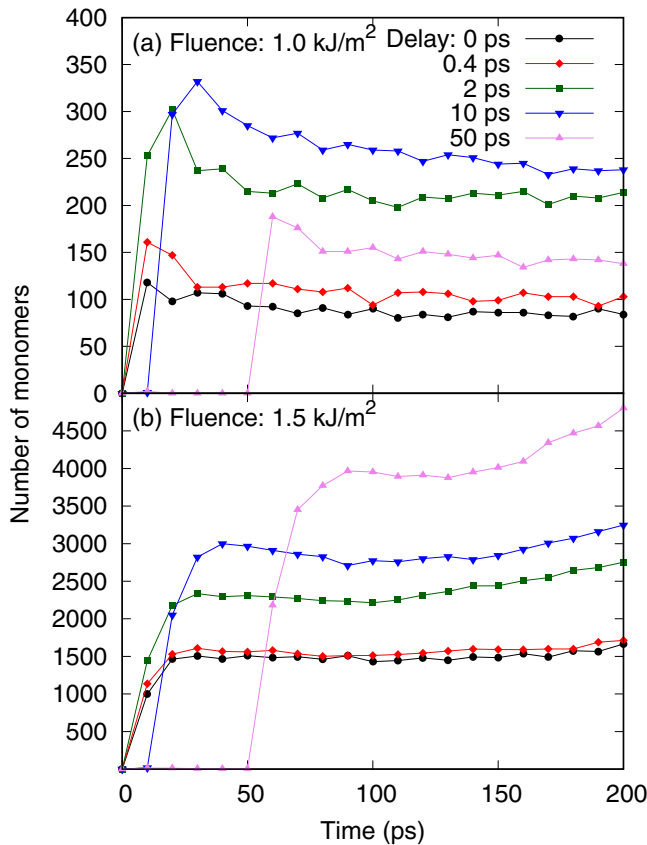


FIG. 3. Number of monomers ejected from the target as a function of time after irradiation at a fluence of (a) 1.0 kJ/m² and (b) 1.5 kJ/m² for different DP delays.

and DP delays 0.4 and 2.0 ps, sizable subsurface voids, which reach a maximum size 140 ps after the first pulse, develop. At intermediate fluence, 1.0 kJ/m², the growth of subsurface voids leads to spallation, except at 50 ps delay for which they reach a limiting, maximum size about 140 ps after the first pulse. This process—the ejection of entire substrate layers—is known as spallation [74,75]. As discussed in Sec. IIC, this process may be accelerated due to the finite size of the simulation volume. At a fluence of 1.5 kJ/m², finally, several voids nucleate and grow rapidly, which eventually leads to the formation of many fragments of a smaller size compared to those released at intermediate fluence. At this fluence, the ejection of single Al atoms becomes more important, especially at larger delays.

At such “low” fluences—i.e., well within the thermal regime—vaporization is responsible for only a small portion of the ablated material. The number of monomers ejected from the target as a function of time is shown in Fig. 3. Clustering of atoms is based on a simple distance criterion of 3.2 Å. For an absorbed fluence of 0.5 kJ/m², vaporization is negligible, independently of delay (data not shown). For fluences twice and three times as high, vaporization levels increase by one or two orders of magnitude or more, respectively. Even though fluence is clearly the most important factor in determining vaporization levels, a carefully chosen DP delay yields a twofold increase in vaporization with respect to SPs. Vaporization levels increase monotonically for delays up to 10 ps and 50 ps at fluences

of 1.0 kJ/m² and 1.5 kJ/m², respectively. Furthermore, we note that vaporization takes place almost completely following the second pulse. The highest levels are achieved if the first pulse is already above the ablation threshold, and the second pulse arrives at a moment when some pieces of material have already detached, forming a foamy structure at the surface (see Ref. [73]). This leads to a particularly large overall surface area (liquid-gas or liquid-vacuum interface) and enough room for the material to expand, which favors vaporization. Eventually, the vaporized atoms may coalesce, and this explains the decline of some of the curves at larger times.

As Fig. 2 shows, larger clusters with more than ten atoms are very limited in number so that statistically relevant information can hardly be extracted. This is due to limitations imposed by the lateral dimensions of the system. Even though very small, the number of such larger clusters appears to increase with fluence. The speed of ejection of the fastest fragments does not vary much with DP delay, and seems to depend only on fluence: averaged over the different DP delays probed here, values of 2.5, 5.8, and 8.7 km/s are obtained for fluences of 0.5, 1.0, and 1.5 kJ/m², respectively. The trend of the nanoparticle population of shifting to lower sizes persists at larger fluences due to plume reheating when the first laser pulse is above the ablation threshold [47]. Ablation experiments on metals also show that the size of ejected fragments decreases with DP delay [20]. While our statistics are insufficient to confirm this, we note that certainly the number of single atoms increases with delay at a fluence of 1.5 kJ/m². Furthermore, smaller fragments are deposited over larger areas of the sample [54]; this manifests an inverse correlation between ejection speed and fragment size.

For LIBS applications, it is essential that the single-atom component of the ablated material be maximized in order to show clear spectral lines that are missing in the blackbody-like continuum from NPs [76]. As described in the previous paragraph, the use of DPs increases the number of single atoms in the ablation plume without increasing overall matter removal, thus improving spectral resolution while limiting the damage inflicted to the target. Indeed, ion yield [43] and spectrally resolved plasma emission [31,77] were found to be enhanced as the DP delay is increased from 0 to tens of ps. Our results are consistent with these findings and we discuss the thermodynamic reasons behind them—enhanced vaporization at larger DP delay and fluence—in the following.

B. Thermal effects on the target

Homogeneous melting at the surface of the target sets in several ps after the laser irradiation. Figure 4 shows the position of the solid-liquid interface as a function of time for various DP delays and fluences of 0.5 (upper panel) and 1.5 kJ/m² (lower panel). A portion of the target is declared to be in a liquid state when the average of the centrosymmetry parameter of its atoms exceeds 20 Å². The melting depth does not depend very much on delay, only on fluence. Averaged over the different delays and for fluences of 0.5, 1.0, and 1.5 kJ/m², the melting depth reaches 0.09, 0.15, and 0.19 μm, respectively, after 200 ps—see inset of Fig. 4(b)—displaying a slightly sublinear increase with fluence. As Fig. 4 reveals, two phases of melting can be identified: the first one is fast

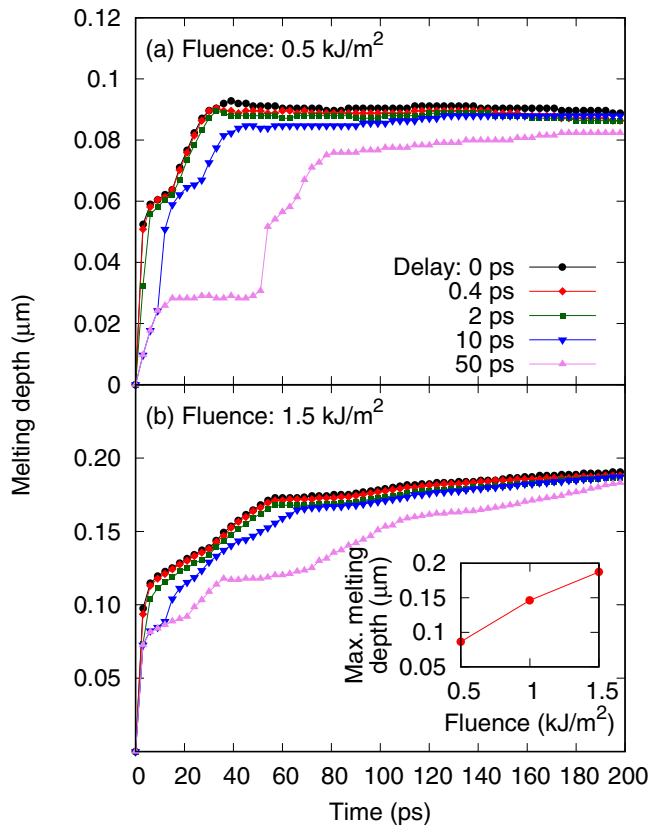


FIG. 4. Position of the solid-liquid interface as a function of time for different DP delays, for fluences of (a) 0.5 and (b) 1.5 kJ/m^2 . The thermodynamic state (liquid or solid) is assigned based on a threshold of 20 \AA^2 of the average centrosymmetry parameter for atoms within cells of edge lengths $\approx 0.8 \text{ nm}$. The inset of panel (b) shows the melting depth (averaged over the different values of delay) 200 ps after the first pulse as a function of fluence.

and due to the rapid transfer of heat from the electrons and the subsequent homogeneous melting of the solid; the second phase occurs under the influence of the rarefaction wave, as will be discussed in Sec. III C.

Figure 5 shows the peak ionic and electronic temperature as a function of delay for the three series of simulations. Electrons are heated directly by the laser, which explains the essentially linear relation between fluence and electronic temperature; this is also the reason why the highest electronic temperatures occur at the surface of the target. Subsequently, the energy diffuses within the electronic subsystem over larger regions of the target. Thereafter, the electrons transfer their energy to the ionic cores, which causes the electronic temperature to decay, approaching the ionic temperature as the delay increases. The second laser pulse reheats the electrons, which are increasingly “cold” as delay increases, and, therefore, the peak electronic temperature decreases monotonically with delay. The peak electronic temperature coincides with the second pulse, except at the highest fluence and the 50 ps delay where it coincides with the first pulse. At even higher fluences (compared to what is studied here), this trend is reversed: Increasing delay correlates with higher electronic temperatures [47,49]. If the first laser pulse carries enough energy to induce ablation, the

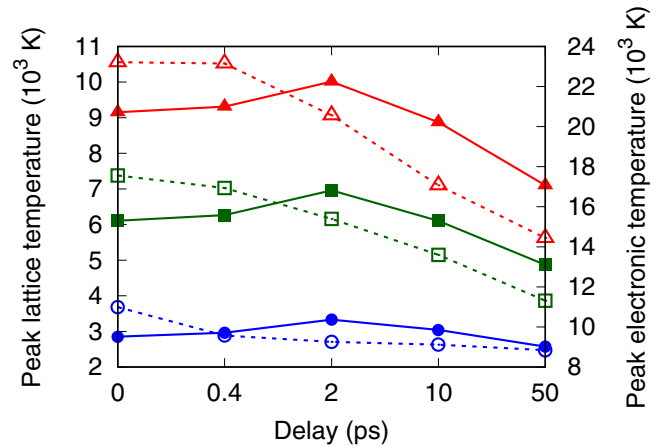


FIG. 5. Peak lattice temperature (full symbols, left scale) and peak electronic temperature (empty symbols, right scale) as a function of delay for absorbed fluences of 0.5 kJ/m^2 (blue circles), 1.0 kJ/m^2 (green squares), and 1.5 J/m^2 (red triangles).

second pulse is mostly absorbed by the ablated material. Due to the lack of contact with the remaining target, the laser energy is concentrated and may heat the electrons in this region to particularly high temperatures.

The highest ionic temperature also follows a linear increase with fluence. Its dependence on delay is more interesting: Heat conductivity in liquid metals is reduced with respect to the solid phase. This, together with the homogeneous melting during the first few ps after the laser irradiation, leads to the concentration of heat in the melted region after the arrival of the second pulse, increasing noticeably the ionic temperature there. However, electron-phonon coupling increases with electronic temperature. Therefore, lower electronic temperatures correlate with slower heating of the atoms, which also leads to lower peak ionic temperatures at higher delays. This reasoning is consistent with the experimental observations of reduced peak lattice temperature as a function of delay [36]. One can speculate that the competition between these two effects leads to the maximum in peak ionic temperature found at a delay of 2 ps.

C. Pressure waves initiated by the ablation process

Pressure profiles as a function of time are shown in Fig. 6 for DP delays of 0 (left column), 10 ps (center column), and 50 ps (right column), and the three fluences considered in the present work. The compression and rarefaction waves are associated with the high and low pressure regions, and travel from the surface into the bulk. The speed of the rarefaction wave is slower than that of the compression wave, and thus their separation increases with time. Despite the shock-absorbing boundary layer, a small, partial reflection of the compression wave at the bottom of the MD cell is visible in Fig. 6; this is an artifact of the simple procedure used for absorbing the shock [67]. Reflection of the pressure waves at the solid-liquid interface is negligible.

In the case of a 10 ps delay, the compression wave generated by the second laser pulse coincides with the formation of the rarefaction wave from the first pulse. Compared to SP ablation

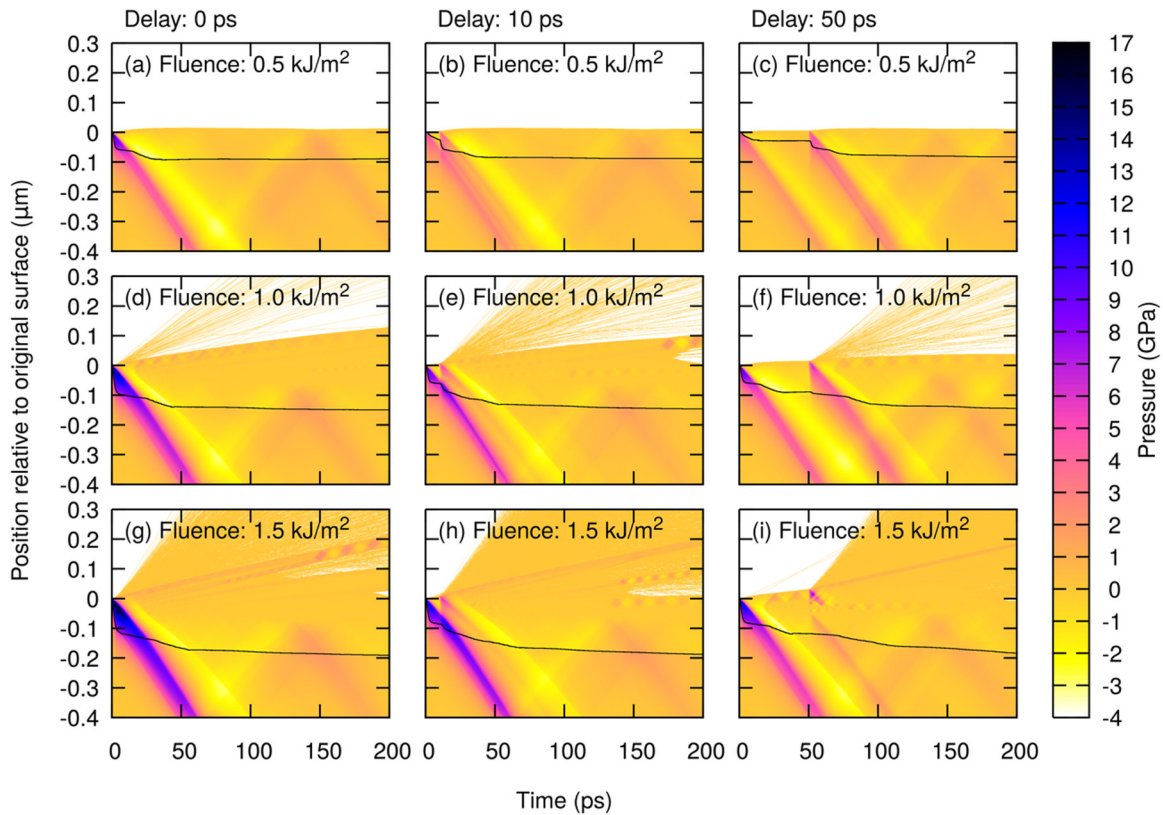


FIG. 6. Pressure profiles as a function of time for an absorbed fluence of 0.5 kJ/m^2 (top row), 1.0 kJ/m^2 (middle row), and 1.5 kJ/m^2 (bottom row), and delays of 0 (i.e., SP; left column), 10 ps (center column), and 50 ps (right column), color-coded according to the pressure scale on the right. The solid line indicates the position of the liquid-solid interface as a function of time.

(left column), this leads to a weaker rarefaction wave from the first pulse and compression wave from the second pulse. Still in comparison with SPs, the time separation between the compression and rarefaction waves increases by about 10 ps. Depending on fluence and delay, spallation occurs between 100 and 200 ps after the first pulse. In the piece of matter that detaches, relatively strong vibrations occur that are accompanied by fluctuations in pressure [Figs. 6(d)–6(i)]. At a delay of 50 ps, two distinct pairs of compression and rarefaction waves develop; i.e., the pulses act as if they were independent. Because the total laser energy is distributed over two pressure waves, they are weaker compared to the SP case. For a fluence of 1.5 kJ/m^2 and a delay of 50 ps, the second pulse interacts mostly with the matter ablated by the first pulse. The second pulse, therefore, does yield only a very weak pressure wave. A similar pressure profile analysis has been carried out by Povarnitsyn and coworkers [49], though at higher laser fluence. Their study shows that the shielding effect remains important at higher fluences, even if the second pulse always generates a noticeable pressure wave in the target. The pressure profiles for delays of 0.4 and 2 ps are very similar to the one for SP ablation.

The highest positive pressures, found at the front of the compression wave, are represented as a function of time in Figs. 7(a)–7(c), for various delays. For delays ≤ 2 ps, the curves show a single maximum, reached within 2–5 ps of the first pulse, at a depth 15–27 nm below the initial surface. As the compression waves travel into the target, their intensities decay to half their peak value in about 20 ps.

For a delay of 10 ps, there is still only one compression wave, as can be appreciated from Figs. 6(b), 6(e) and 6(h). However, as a function of time, two pressure maxima occur, each shortly after the corresponding laser pulse [see Figs. 7(a)–7(c), blue curves]. The peak pressure is about 4.2–4.5 GPa lower as compared to SPs. The second peak pressure appears at a deeper position in the target, 60–90 nm from the surface. After the compression wave has been reinforced by the second pulse, its intensity decays much slower compared to the SP case.

For the 50 ps delay, and for fluences of 0.5 and 1.0 kJ/m^2 , also two pressure maxima occur as a function of time [see Figs. 7(a)–7(c), purple curves]. However, as can be seen in Figs. 6(c) and 6(f), these maxima belong to two different compression waves. This means that the two laser pulses act independently, which explains that the corresponding pressure maxima have values close to the one found for SPs at half the fluence. At the fluence of 1.5 kJ/m^2 and the 50 ps delay, there is only one compression wave which is generated by the first pulse [see Fig. 7(c), purple curve]. The second pulse has little effect on the target: in particular, it does not yield a second compression wave, as ablated matter from the first pulse shields the remaining target [see Fig. 6(i)].

Figures 7(d)–7(e) show the most negative pressures at the front of the rarefaction waves. At delays equal to or below 2 ps, this is in the range of -3.3 to -3.5 GPa, essentially independent of fluence. For such small delays, there is a single rarefaction wave. Likewise, for a delay of 10 ps, only one rarefaction wave occurs for all fluences examined [see Figs. 6(b),

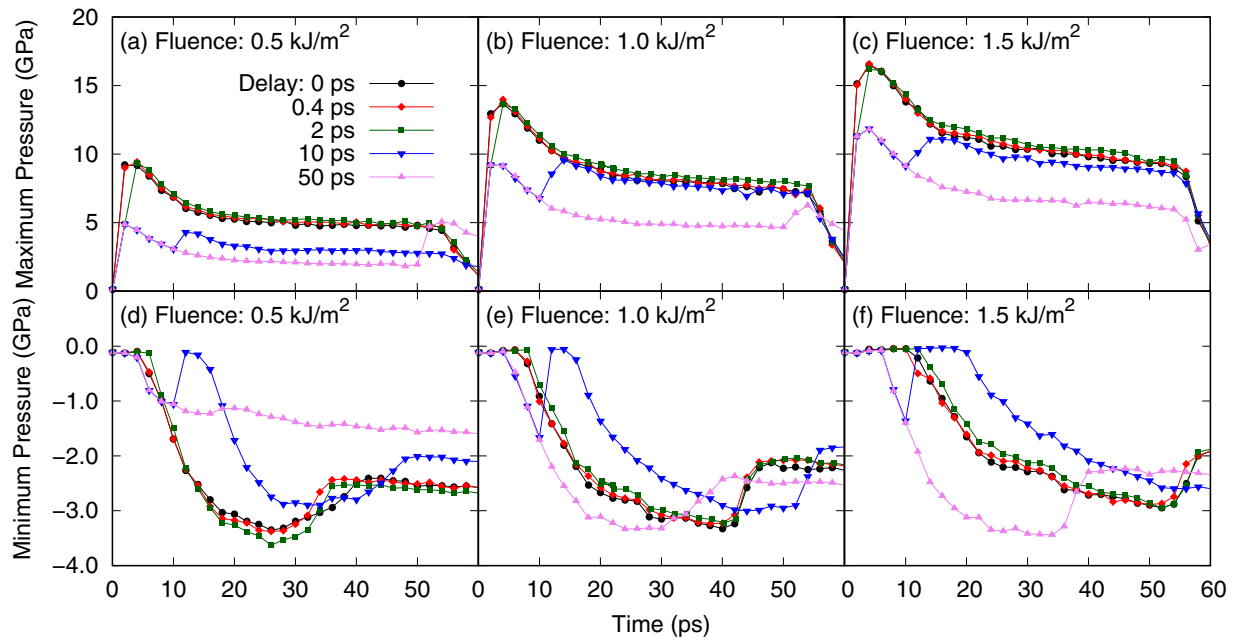


FIG. 7. Highest pressure at the front of the compression wave [panels (a)–(c)] and most negative pressure occurring in the rarefaction wave [panels (d)–(f)] as a function of time for different DP delays and fluences (as indicated).

6(e) and 6(h)]. However, because of the interaction with the compression wave from the second pulse, the rarefaction wave is weaker and lies in the range -2.9 to -3.0 GPa, regardless of fluence. Finally, as was the case for the compression waves, the 50 ps delay leads to two distinct rarefaction waves at fluences of 0.5 and 1.0 kJ/m^2 [see Figs. 6(c) and 6(f)]. Except for the lowest fluence, the most negative pressure found in these waves is similar to that found in the rarefaction waves for SP ablation. This means that, at such large delay, the rarefaction wave from the first pulse is not affected by the second pulse as it has already propagated deeper into the bulk by the time the second pulse arrives. A delay of 50 ps is therefore enough for the formation of two independent pairs of compression and rarefaction waves, provided the fluence is low enough that the second pulse can actually reach the surface and is not shielded by ablated material from the first pulse.

The decrease in intensity of the compression waves at larger delays may help prevent the formation of microcracks [78]. In addition, as noted above, at the 10 ps delay, it appears that the maximum pressure at the front of the compression waves varies much less as a function of time compared to other delays. It may be speculated that the lower stresses combined with the reheating from the second pulse leads to the smoother crater shapes observed in ablation experiments using temporally shaped laser pulses [38,39].

The maximum and minimum pressures as a function of time and position have also been evaluated in order to estimate the propagation speeds of the first compression and rarefaction waves, and these are reported in Fig. 8. During the first 3–5 ps after the first pulse, the speed at which the melted region expands is larger than the speed of the compression wave due to homogeneous melting. Therefore, the compression wave propagates first through the liquid until it overtakes the liquid-solid boundary 60–130 nm below the original surface [see Fig. 6: initially, the high-pressure region (blue

is above the liquid-solid interface (black curve)]. The speed of the compression wave clearly increases, from an average of 5.6 km/s to 7.0 km/s as the wave crosses the phase boundary between liquid and solid. The speed of the compression wave does not significantly depend on DP delay or laser fluence in the parameter range examined here, despite the fact that the intensity of the compression wave correlates strongly with laser fluence [compare Figs. 7(a)–7(c)]. This could explain why the characteristic double-pulse delays that define the regimes observed by Semerok and Dutouquet do not depend on fluence [30].

The speed of propagation of the rarefaction wave decreases significantly with laser fluence because of the higher overall ionic temperatures caused by higher fluences (see also Fig. 5).

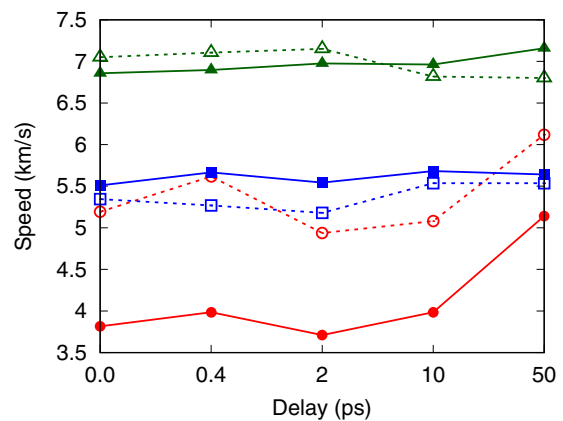


FIG. 8. Propagation speed of pressure waves for various DP delays at a total absorbed fluence of 0.5 kJ/m^2 (empty symbols) and 1.5 J/m^2 (full symbols): compression wave in the liquid (blue squares) and solid (green triangles) parts of the target, and rarefaction wave (red circles).

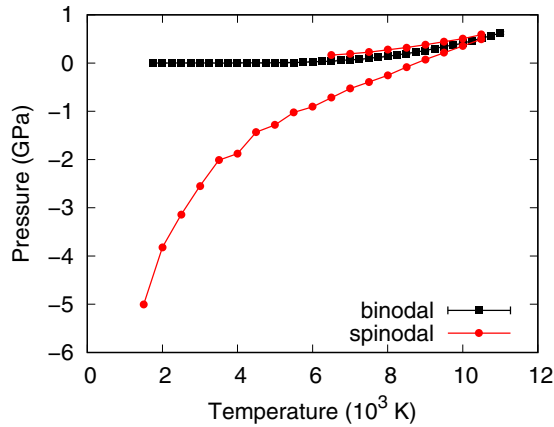


FIG. 9. Liquid-gas binodal (black squares) and spinodal (red circles) curves for Al modeled by the EAM of Zope and Mishin [63] in the temperature-pressure plane.

The dependence on delay of the speed is limited also for rarefaction waves. The higher propagation speed at a delay of 50 ps is explained by the fact that the corresponding rarefaction wave is generated by only half the laser fluence. The rarefaction wave follows shortly (a few ps) after the compression wave. As the rarefaction wave is slower than the compression wave, the time difference increases with depth. Close to the target surface, it is highest for the 10 ps delay, where it reaches 10–20 ps depending on fluence, and smallest for the 50 ps delay, with values of about 5 ps. The reason for this relatively late and weak rarefaction wave [see also Figs. 7(d) and 7(e)], at delay 10 ps, is again the compensation of the rarefaction wave from the first pulse by the compression wave of the second pulse. Therefore, the rarefaction wave that remains is the one from the second pulse and it develops about 10 ps—the amount of time of the delay—later. The rate of decompression, from the peak pressure of the compression wave to the most intense negative pressure of the rarefaction wave, is consequently reduced at a delay of 10 ps. Although we did not investigate the dependence of the size distribution of droplets, it is likely that the rate of decompression affects phase explosion and the properties of the mixture of gas and droplets it produces. Therefore, varying delays could be a way to control the size distribution of ablation-generated NPs.

D. Thermodynamic pathways and cavitation

In order to assess the thermodynamic stability of different portions of the target as a function of time, the binodal and spinodal lines for the present EAM potential for Al have been calculated. Figure 9 shows these lines in the temperature-pressure plane; details of the calculations are given in Appendix B 1. For the ablation simulations, the stability of the overheated liquid is of interest: the rarefaction wave, with strong negative pressure at its front, travels through hot liquid material from homogeneous melting. This means, depending on the precise values of temperature and pressure, that the liquid may enter the metastable region between the binodal and spinodal (between the black and lower red lines in Fig. 9). The likelihood of phase explosion, the decomposition of a thermodynamically metastable homogeneous liquid into a mixture

of liquid droplets and gas, increases as the liquid approaches the spinodal line [5,79]. In principle, metastable states may also be reached when a supercritical fluid expands (fragmentation) [57]; however, in the simulations reported here, the material never becomes supercritical, which proscribes this ablation mechanism in the present context.

During the simulations, the pressure and temperature throughout the target were recorded, allowing us to follow the thermodynamic pathways of different portions of it through the phase diagram during the ablation process. As an illustration, Fig. 10 shows such pathways in the temperature-pressure plane for delays of 0 (SP), 10, and 50 ps, for the first 100 ps following the first pulse at a fluence of 1.0 kJ/m². For each delay, pathways of ten 14.5-nm-thick slabs from the top portion of the target, thus reaching from the surface down to 145 nm into the bulk, are presented.

We first discuss the 0 ps delay case, i.e., SP ablation [Fig. 10(a)]. All pathways start at room temperature and zero pressure (left bottom corner of the diagram). Under the influence of the laser pulse (indicated by a black circle at the beginning of the pathway), temperature and pressure both rise with time. The highest temperatures are reached at the surface, i.e., where the laser is most intense. The highest pressures are obtained slightly below the surface because the top slice (0–14.5 nm) can expand into vacuum, thus reducing pressure buildup there. In comparison to the peak temperature, the peak pressure decreases much slower with depth because pressure is more easily “transmitted” over large distances via compression waves. Except for the top slice, the density of the material remains constant during this first part of the thermodynamic pathway, until the maximum pressure is reached. Thereafter, during the time interval between the passage of the compression and rarefaction waves, the pressure drops rapidly while the system also slowly cools down. This continues until the material crosses the liquid-gas binodal (dashed line) and enters a thermodynamically metastable state. Several slices enter deep into this region, even approaching the spinodal line, increasing the probability of phase explosion. In the following, we discuss the probability of nucleation of bubbles in more detail. If phase explosion occurs in a given region of the target, pressure increases up to the binodal line for both liquid and gas fractions. If phase explosion does not take place, negative pressure in the liquid is relaxed after the passage of the rarefaction wave and the material continues to cool, so that it also approaches the liquid-gas binodal. Despite a rather different model, we note close quantitative agreement with Wu and Zhigilei in the SP case [18]. In addition, the system size in Ref. [18] is much larger compared to the one considered here. This agreement demonstrates the robustness of the MD-TTM approach with respect to details of the model.

Splitting the laser energy over two pulses changes the thermodynamic trajectories, and this depends on the precise moment of arrival of the second pulse. The pathways for DPs with delays of 0.4 ps to 2 ps resemble those for SPs very much (not shown). For a 10 ps delay, the second pulse strikes the target while the pressure is decreasing rapidly within the top layers [Fig. 10(b), black circles]. This stops the drop in pressure and prevents most of the target from becoming metastable. The second pulse heats up the target again to even higher temperatures, exceeding those obtained during SP ablation.

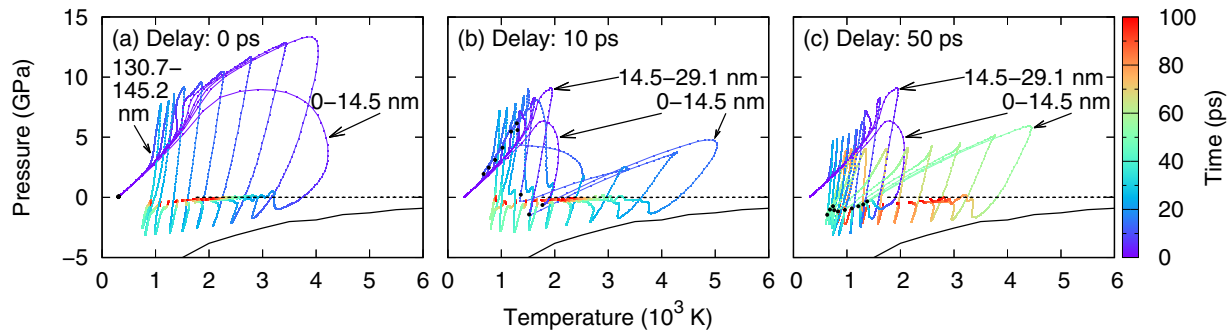


FIG. 10. Thermodynamic pathways of ten 14.5-nm-thick slices from the top 145 nm of the target, following irradiation with a DP with total absorbed fluence 1.0 kJ/m^2 , during the first 100 ps following the first pulse, for delays 0 ps [i.e., SP, panel (a)], 10 ps (b), and 50 ps (c). For clarity, some of the pathways are labeled according to the region in the target to which they belong. Neighboring pathways correspond to neighboring regions in the target. The curves that reach the highest temperatures belong to the top part of the target and lower maximum temperatures are found deeper into the target. The black circles mark the arrival of the second laser pulse. The liquid-gas binodal and spinodal are shown as black dashed and continuous lines, respectively (cf. Fig. 9).

The maximum pressure remains significantly below the values reached shortly after the first pulse.

At a 50 ps delay, the second pulse [Fig. 10(c), black circles] arrives at the target when the material has already passed through the metastable region of the phase diagram. Depending on position (depth) and fluence, either phase explosion has taken place and the material decomposed into a mixture of liquid and gas at the binodal line, or the pressure in the liquid has relaxed back to zero after the passage of the rarefaction wave from the first pulse. In either case, pressure is close to zero and temperatures have started to decline. The material, therefore, even though at higher temperatures and in liquid state, is not very far from the initial condition. Consequently, the second pulse causes the target to cycle a second time through the thermodynamic pathway for SP ablation (at half the fluence) described above. During this second cycle, the overall temperature is higher and the maximum pressure is reduced.

The pathways obtained at fluences of 0.5 kJ/m^2 and 1.5 kJ/m^2 (not shown) display a similar behavior: The overall forms of the pathways are essentially the same; only maximum temperature and pressure vary, as can also be appreciated from Figs. 5 and 7, respectively. In addition, at the fluence of 1.5 kJ/m^2 and the delay of 50 ps, the spalled top portion of the target gets affected most by the second pulse. Therefore, only this part is heated again and the remainder of the target follows pathways similar to those for SP ablation.

The portions of the target in the metastable region of the phase diagram may undergo explosive decomposition. The probability of such an event is given by the cavitation rate J —the nucleation rate of bubbles or voids in the liquid—which can be estimated by classical nucleation theory [80]:

$$J = N \sqrt{\frac{2\sigma(T)}{\pi m}} \exp\left(-\frac{16\pi[\sigma(T)]^3}{3k_B T [P_V - P_L]^2}\right) \quad (8)$$

with N the atomic number density, m the mass of an atom (here Al), k_B the Boltzmann constant, T the temperature, $\sigma(T)$ the surface tension, and P_V and P_L the pressures in the vapor and liquid phases, respectively. Considering the large negative pressures occurring in the liquid, it is justified to neglect P_V with respect to P_L . Visual inspection of snapshots from the simulations also shows that the bubbles are mostly empty. In

order to evaluate this expression, the surface tension of Al as a function of temperature for the present EAM potential has been calculated (see Appendix B 2). Cavitation is limited to the liquid part of the target, the region delimited by the melting depth curve of Fig. 4. Additionally, cavitation requires the pressure in the liquid to be lower than the vapor pressure at that temperature. In this liquid region, the cavitation rate may vary over several orders of magnitude as both pressure and temperature appear in the exponential in Eq. (8). This limits cavitation to the time frame of the passage of the rarefaction wave.

Cavitation rates obtained in this way have been integrated over the entire target and over the full simulated time, yielding the number of expected bubble nucleation events throughout the simulation volume. The results are shown in Fig. 11. The overall number of nucleation events evidently increases with laser fluence but depends significantly on delay: cavitation is highest for intermediate delays (2.0–10 ps depending on fluence). The highest overall bubble formation rate is however found at a delay of 50 ps at the highest fluence. This high

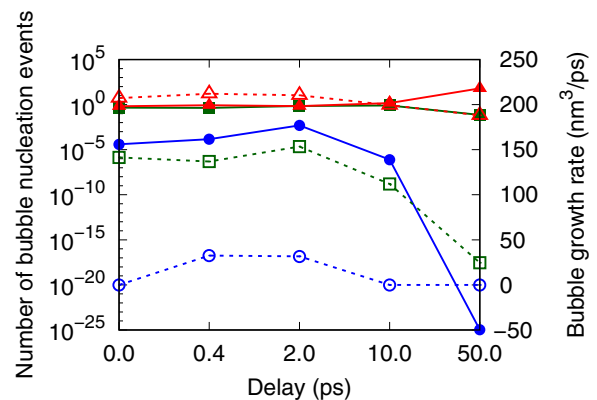


FIG. 11. Number of bubble nucleation events inside the simulation volume as predicted by classical nucleation theory (full symbols, left scale) and average bubble growth rate (empty symbols, right scale) 60–100 ps after the first pulse, as a function of delay for total absorbed fluences of 0.5 kJ/m^2 (blue circles), 1.0 kJ/m^2 (green squares), and 1.5 J/m^2 (red triangles).

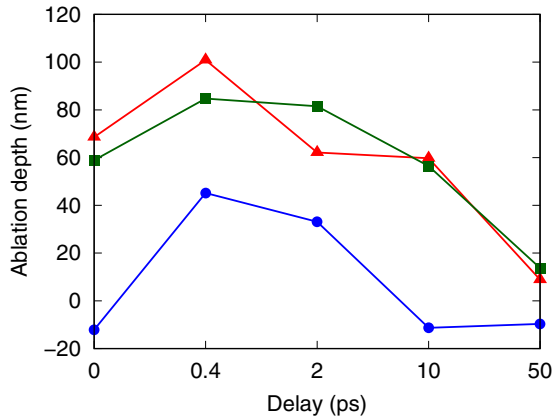


FIG. 12. Ablation depth after 200 ps following the impact of the first laser pulse as a function of DP delay for total absorbed fluences of 0.5 kJ/m^2 (blue circles), 1.0 kJ/m^2 (green squares), and 1.5 kJ/m^2 (red triangles).

cavitation rate is limited to a small portion of the system, viz., the already-spalled material from the first pulse. This chunk gets broken down into smaller pieces by explosive boiling induced by the second pulse, which explains the increase in the number of vaporized atoms seen in Fig. 3 at that fluence and delay.

The growth rate of the volume of subsurface voids created by explosive boiling as a function of delay is also shown in Fig. 11. In order to identify individual voids, the “surface mesh feature” of the OVITO software is used [81] (with a probe sphere radius of 3.2 \AA). From that we obtain the total volume of all bubbles present in the target, and comparing with subsequent simulation snapshots allows us to estimate the growth rate of the total bubble volume. The growth rate is highest between 60–100 ps following the first laser pulse and close to constant for all the simulations reported here. Figure 11 shows the average value of the growth rate of the total bubble volume during that time interval. The results exhibit a behavior qualitatively similar to the number of bubble nucleation events, indicating that the above approach, based on classical nucleation theory, can indeed predict the rate of formation of bubbles in the target. If the growth rate of the total bubble volume is below $50 \text{ nm}^3/\text{ps}$, spallation does not occur, consistent with the vanishing probability of bubble formation predicted by classical nucleation theory in these cases. In the case of the highest fluence and largest delay, bubble growth rates are limited by the small size of the pieces of matter in which the bubbles form.

The ablation depth, displayed in Fig. 12, or equivalently the amount of ablated material (ablation yield), exhibits a maximum at a small delay of 0.4 ps. Higher values of the delay lead to a decrease in ablation depth even below the level for SP ablation. In our simulations, the ablation depth does not increase any further after about 110 ps following the arrival of the first laser pulse. We carried out two simulations (fluence 1.0 kJ/m^2 and delays 0 and 50 ps) up to 500 ps after the first laser pulse and found no further spallation event to occur (not shown). On the contrary, due to cooling and recondensation of atomic gas at the target surface, the ablation depth decreases, but this effect is minute. This relatively fast convergence to the final ablation depth is most likely due to the finite simulation volume: If

bubbles outgrow the system dimensions, artificially fast spallation occurs (see also the discussion in Sec. II C). This decrease in ablation depth has already been reported in experimental work [30,46,76] for similar DP delays. In simulations, Povarnitsyn and coworkers also found a reduction of crater volume in the case of DP with respect to SP ablation, and attributed it to the compensation of the rarefaction wave from the first pulse by the compression wave from the second pulse [45–47,49]. A peak ablation depth at nonzero delay, as we find here, has also been mentioned in experimental [51] and numerical [48] studies. The detailed analysis of the pressure waves above confirms these results. However, at larger delays and higher fluences, the shielding of the target by already-ablated material becomes a more important factor in reducing the ablation yield. As it absorbs most of the energy of the second pulse, this spalled portion of the target becomes particularly hot. When it detaches from the remaining target, it carries thermal energy away in a process known as ablation cooling [82].

A SP at fluence 0.5 kJ/m^2 is just below the ablation threshold. Ablation can still be achieved at this fluence by splitting the laser energy into two pulses with delays between 0.4 and 2.0 ps. We define the ablation depth as the difference between the initial and final position (after 200 ps following the first pulse) of the surface of the target; this can be negative if the final position of the surface is “above” the initial one because, e.g., of disorder and/or nanovoid formation during ablation. This is the case for the 0.5 kJ/m^2 fluence, for delays of 0, 10, and 50 ps. Even though the simulations were not carried out until resolidification of the target surface, we speculate that subsurface structures formed following the laser pulses, then freeze out and can thus be associated with surface swelling [18,61,83,84]. Doubling the laser fluence to 1.0 kJ/m^2 increases the ablation depth significantly; however, a further increase in fluence does not increase the ablation depth here.

IV. CONCLUSIONS AND OUTLOOK

The effect on the ablation process of ultrashort DPs with delays in the range of 0–50 ps has been studied using a hybrid TTM/MD approach. DP delay turns out to be an important parameter for controlling ablation by the enhancement of certain mechanisms, as shown in Table I and discussed below.

Vaporization, or the collective ejection of monomers (or very small clusters), is amplified by increasing the DP delay even though overall levels remain low in all simulations reported here. A high number of monomers in the ablation plume may improve the resolution and intensity of emission spectra making DP ablation interesting for the LIBS measurements [31,55,85,86]. In addition, our simulations at a fluence of 1.5 kJ/m^2 , the largest considered here, show that the ablated matter shields the remaining target from further ablation. This is a promising condition for LIBS applications where the damage to the target needs to be minimized.

The properties of ablation pressure waves also depend strongly on delay. At delays of 2 ps or less, only one pair of compression and rarefaction waves is generated. At a delay of 10 ps still only one pair of waves propagates through the target, but the time separation between the compression and rarefaction wave increases and their intensity is very

TABLE I. Overview of the dominant ablation phenomena for all the values of DP delay and laser fluence probed in the present study.

Delay	Phenomena at laser fluence values of		
	0.5 kJ/m ²	1.0 kJ/m ²	1.5 kJ/m ²
0 ps	Highest electronic temperatures at all three values		
0.4 ps	Ablation depth maximized at all three values		
2 ps	Largest peak lattice temperatures at all three values		
10 ps	Rarefaction wave from 1st pulse compensated by compression wave from 2nd pulse at all three values		
50 ps	Cavitation rate reduced	Cavitation rate reduced	Ablated matter of 1st pulse shields target from 2nd pulse; vaporization maximized

much reduced as the compression wave from the second pulse compensates the rarefaction wave from the first pulse. This is in agreement with earlier simulations by Povarnitsyn and coworkers [45–47,49]. Moreover, the second pulse hits a hot and dilated target when it arrives at least 10 ps after the first pulse, further reducing the intensity of both compression and rarefaction waves. Finally, at a delay of 50 ps and high fluence (1.5 kJ/m²), ablated matter from the first pulse shields the remaining target and thus prevents the development of a second pair of compression and rarefaction waves. At lower fluences, the laser energy is distributed over two compression waves, thus reducing peak pressure.

In the cases where the intensity of the rarefaction wave is reduced, for one of the reasons cited above, cavitation rates and thus the growth of subsurface voids is also reduced. In this way, by choosing delays of the order of tens of ps, phase explosion and spallation may be minimized. This leads to a decrease in the overall ablation yield seen in Fig. 12 in this delay regime, corroborating experimental work [30,46,76].

Even though ablation yield decreases with delay, the melting depth does not—it appears to depend on fluence only. This is consistent with other numerical work [48]. Interestingly, our simulations indicate that peak lattice temperatures, cavitation rates, and ablation yields may be slightly higher in the case of DPs with very short delays (0.4–2 ps) as compared to SPs. While the effect is small, a similar trend has been found in other studies already [48,51]. Peak temperatures and pressures are found to be reduced in the case of larger DP delays (10 and 50 ps). This explains in part why ablation craters are smoother and microcracks are reduced in this delay regime [38,39,78].

As a possible extension, asymmetric DPs could be studied as a means to further improve control over the ablation process [48,87]. Investigating more general pulse shapes [88], the laser fluence could also be adjusted in real time, in order to limit temperature or pressure buildup in the target, or to drive certain portions of the target deliberately into phase explosion. This way, pulse shapes could be designed for the enhancement of a particular ablation mechanism. Work in this direction is underway.

ACKNOWLEDGMENTS

This work was supported by grants from the Natural Sciences and Engineering Research Council of Canada (NSERC) and the Fonds de Recherche du Québec—Nature et Technolo-

gies (FRQ-NT). We are indebted to Calcul Québec and Calcul Canada for generous allocations of computer resources.

APPENDIX A: DETAILS OF THE MODEL FOR THE ELECTRONIC HEAT CONDUCTIVITY OF INOGAMOV AND PETROV

The formulation for the electronic heat conductivity $K_e(T_e, T_i)$ in the present model is largely borrowed from Inogamov and Petrov [1]:

$$K_e(T_e, T_i) = \frac{2C_e(T_e)E_e^{\text{kin}}(T_e)\tau_{\text{eff}}(T_e, T_i)}{3m_e}, \quad (\text{A1})$$

where m_e is the mass of the electron. In their work, they present a model, valid over a wide range of T_e and T_i (up to several 10 000 K), for the effective collision time τ_{eff} that we use here. However, instead of their approximation for the average kinetic energy of the electrons E_e^{kin} , we derive this quantity from the heat capacity C_e computed by Lin and coworkers [64],

$$E_e^{\text{kin}}(T_e) = \int_0^{T_e} C_e(T) dT + \frac{3E_F}{5}, \quad (\text{A2})$$

where $E_F = \frac{\hbar^2}{2m_e} (3\pi^2 Z N_0)^{2/3}$ represents the Fermi energy that is calculated for $Z = 3$ conduction band electrons in Al and its atomic number density of $N = 6.02 \times 10^{28}$ 1/m³ in normal conditions. We chose this approach in order to be more consistent with the remainder of the electronic heat equation which also features this model for the electronic heat capacity.

We adopt the collision time τ_{eff} , depending on electron-electron and electron-ion collision frequencies, of the “wide-range” model by Inogamov and Petrov without any modification [1]. In their formulation, electron-ion collision frequencies depend on the thermodynamic state of the material. We use the average value of the centrosymmetry parameter of the atoms in a given cell in order to determine whether it is in a solid or liquid phase, using a threshold of 20 Å². Cells beyond the MD region are assumed to remain in the crystalline solid phase.

APPENDIX B: PHASE DIAGRAM AND SURFACE TENSION OF Al

For the interpretation of the ablation simulations it is crucial to know the properties of Al, especially at high temperatures, as modeled by the present EAM potential of Zope and Mishin [63]. The liquid-gas spinodal and binodal as well as the surface

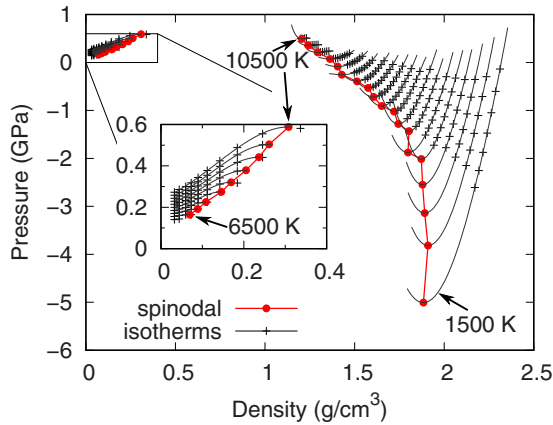


FIG. 13. Isotherms in the density-pressure plane for Al as obtained in a series of canonical EAM-based MD simulations at temperatures ranging from 1500 to 10 500 K at 500 K intervals. Cubic polynomials (black lines) have been adjusted to the data points (black crosses) in order to extrapolate to the absolute limit of stability of both the gas and liquid phase. This limit defines the spinodal curve (red circles).

tension have been evaluated at temperatures up to the critical point.

1. Phase diagram

A phase diagram is invaluable for the analysis of laser ablation simulations [57]. Since temperature and pressure are known throughout the simulations, comparison with the phase diagram allows us to assess the evolution of the thermodynamic state of the material as a function of location in the target. Unfortunately, the phase diagram is not very well known experimentally in the extreme conditions that occur during the ablation process. Additionally, the EAM has been adjusted to the zero-temperature properties of Al and it is therefore unclear how it performs at conditions close to the critical point. In two series of simulations, we have determined the liquid-gas binodal and spinodal of Al within the EAM model.

Gibbs ensemble Monte Carlo (MC) simulations are employed in order to calculate the liquid-gas binodal line using the Towhee simulation program [89]. As initial configuration, two boxes with 1000 atoms each were used. During the simulations, volume and particles are exchanged between the two boxes, but the total density remains constant. When the simulation reaches equilibrium, one box contains the gas phase and the other the liquid phase, as long as the total overall density is composed of the densities of the gas and liquid at the given temperature. The series of simulations was therefore started at low temperature (1750 K), keeping the total density always between that of the gas and that of the liquid in the simulation at the next higher temperature. The series of simulations ends at the critical point where these two densities converge.

The simulations were carried out over 22 000 MC cycles, of which the last 2000 have been partitioned into 20 blocks for the calculation of thermodynamic averages. One cycle consisted of 1 translational move of the atoms plus 1 additional volume move, 40, 50, and 60 aggregation volume bias moves of 3 different types, and 60 configurational-bias moves every 100 cycles.

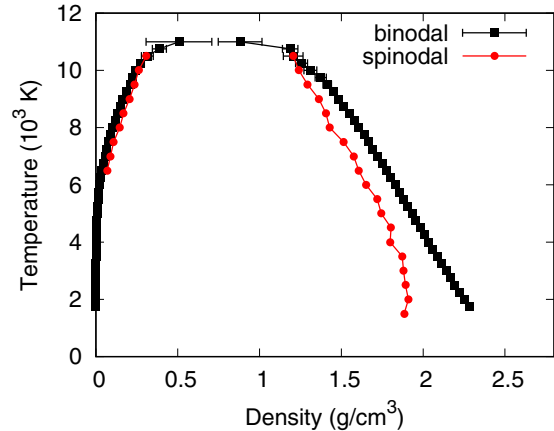


FIG. 14. Liquid-gas binodal (black squares) and spinodal (red circles) curves for Al modeled by the EAM potential of Zope and Mishin [63] in the density-temperature plane.

The spinodal line was subsequently determined in 19 series of canonical ensemble MD simulations at temperatures in the range of 1500–10 500 K. At each temperature, simulations were carried out at several densities close to those of the binodal line, slightly larger densities for the liquid branch and slightly smaller ones for the gas branch in order to ensure stability against explosive decomposition. During these simulations, the pressure was recorded and a third-order polynomial was adjusted to the liquid and the gas branch of each of the 19 isotherms obtained that way. In the case of the gas and liquid branch, the spinodal line can be recovered by connecting the maxima and minima of the polynomials, respectively [90]. This procedure is illustrated in Fig. 13.

With these data at hand, it is possible to draw the liquid-gas phase diagram of Al modeled by the EAM potential of Zope and Mishin. Figure 14 shows the liquid-gas binodal and spinodal lines in the density-temperature plane. The thermodynamic pathway analysis of the ablation simulations is carried out in the temperature-pressure plane, and the phase diagram in that plane is shown in Sec. III D. From this diagram, the critical point is estimated to be at a temperature of $11.5\text{--}12.0 \times 10^3$ K, a density of $0.5\text{--}1.0$ g/cm³, and a pressure of $0.6\text{--}0.7$ GPa. Experimental values of these high-temperature properties are rather dispersed. By comparing a large number of studies, Morel and coworkers concluded that the best experimental estimate for the critical temperature is $T_c = (6700 \pm 800)$ K [91]. This is clearly below what is predicted by the present EAM.

2. Surface tension

In order to evaluate cavitation rates, we need to obtain the surface tension $\sigma(T)$ as a function of temperature for the EAM used in this study. This information is obtained in a series of MD simulations in the canonical ensemble. The initial configuration was set to a cubic block containing $10 \times 10 \times 10$ fcc unit cells (4000 atoms). The system has been placed in a periodic simulation box imposing an overall system volume of $4.05 \times 4.05 \times 20.25$ nm³. The remainder of the simulation box was left empty. The simulation was carried over 0.6 ns, the first 100 ps being disregarded as equilibration period. Simulations in which the initial Al block disintegrated into

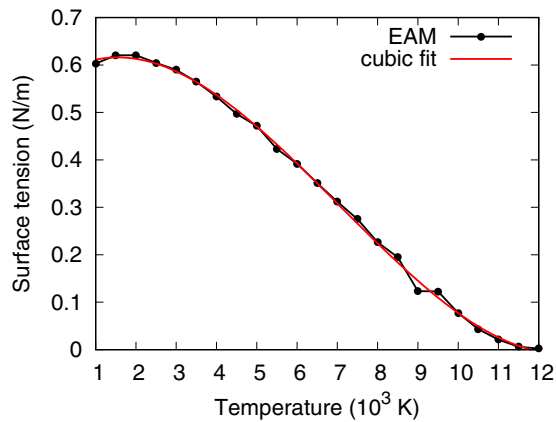


FIG. 15. Surface tension of liquid Al obtained from EAM-based [63] MD simulations as a function of temperature ranging from the melting temperature up to the critical temperature.

smaller fragments were disregarded as their total surface area is larger than twice the lateral cross section of the simulation box. The system has been partitioned into slabs of a thickness of $\Delta z = 0.81$ nm. In these slabs, the diagonal elements of the pressure tensor, P_{xx} , P_{yy} , and P_{zz} , have been evaluated, which allows us to compute the surface tension σ [92]:

$$\sigma = \frac{1}{2} \Delta z \sum_i \left[P_{zz}^i - \frac{1}{2} (P_{xx}^i + P_{yy}^i) \right]. \quad (\text{B1})$$

Figure 15 shows the surface tension of liquid Al modeled by the present EAM [63] as a function of temperature. At zero temperature, the surface tension for this model has been evaluated to be 0.6–0.8 J/m² depending on the fcc crystal orientation [63]. Experimental values for the surface tension of Al are usually limited to temperatures close to the melting temperature [93]. In addition, the surfaces may be affected by the atmosphere. In particular, oxidizing conditions may reduce surface tension [94,95]. Experimental results are often expressed as a linear function of temperature: Under oxygen-reduced conditions, surface tension values of 0.88 [94], 0.98 [95], and 0.99 N m⁻¹ [93] have been reported at the melting temperature of $T_m = 933$ K decreasing with temperature at rates of 0.185, 0.271, and 0.127 mN m⁻¹ K⁻¹, respectively. While the EAM potential reproduces the surface tension around the melting temperature reasonably well, the rate at which it decreases with temperature appears too low. This points again to the fact that the critical temperature is overestimated by this EAM. In particular, in the MD simulations, the surface disintegrates only at temperatures as high as 12 000 K.

In order to make the calculation of cavitation rates more practical, we have adjusted a cubic polynomial (red curve in Fig. 15) that approximates the surface tension of Al for the present interatomic potential:

$$\begin{aligned} \sigma(T) = & 9.348 \times 10^{-13} \text{ N m}^{-1} \text{ K}^{-3} \times T^3 \\ & - 1.977 \times 10^{-8} \text{ N m}^{-1} \text{ K}^{-2} \times T^2 + 5.441 \\ & \times 10^{-5} \text{ N m}^{-1} \text{ K}^{-1} \times T + 0.5757 \text{ N m}^{-1}. \quad (\text{B2}) \end{aligned}$$

- [1] N. A. Inogamov and Y. V. Petrov, Thermal conductivity of metals with hot electrons, *J. Exp. Theor. Phys.* **110**, 446 (2010).
- [2] D. Perez and L. J. Lewis, Molecular-dynamics study of ablation of solids under femtosecond laser pulses, *Phys. Rev. B* **67**, 184102 (2003).
- [3] L. J. Lewis and D. Perez, Laser ablation with short and ultrashort laser pulses: Basic mechanisms from molecular-dynamics simulations, *Appl. Surf. Sci.* **255**, 5101 (2009).
- [4] L. V. Zhigilei, Z. Lin, and D. S. Ivanov, Atomistic modeling of short pulse laser ablation of metals: Connections between melting, spallation, and phase explosion, *J. Phys. Chem. C* **113**, 11892 (2009).
- [5] P. Lorazo, L. J. Lewis, and M. Meunier, Short-Pulse Laser Ablation of Solids: From Phase Explosion to Fragmentation, *Phys. Rev. Lett.* **91**, 225502 (2003).
- [6] D. H. Lowndes, D. B. Geohegan, A. A. Puretzky, D. P. Norton, and C. M. Rouleau, Synthesis of novel thin-film materials by pulsed laser deposition, *Science* **273**, 898 (1996).
- [7] P. R. Willmott and J. R. Huber, Pulsed laser vaporization and deposition, *Rev. Mod. Phys.* **72**, 315 (2000).
- [8] Y. Nakata, J. Muramoto, T. Okada, and M. Maeda, Particle dynamics during nanoparticle synthesis by laser ablation in a background gas, *J. Appl. Phys.* **91**, 1640 (2002).
- [9] G. D. Förster, M. Girault, J. Menneveux, L. Lavissee, J.-M. Jouvard, M. C. Marco de Lucas, V. Potin, F.-X. Ouf, M. Kerkar, J.-L. Le Garrec, E. Carvou, S. Carles, F. Rabilloud, F. Calvo, J. Yu, and J. B. Mitchell, Oxidation-Induced Surface Roughening of Aluminum Nanoparticles Formed in an Ablation Plume, *Phys. Rev. Lett.* **115**, 246101 (2015).
- [10] S. Amoruso, G. Ausanio, R. Bruzzese, M. Vitiello, and X. Wang, Femtosecond laser pulse irradiation of solid targets as a general route to nanoparticle formation in a vacuum, *Phys. Rev. B* **71**, 033406 (2005).
- [11] G. Ausanio, S. Amoruso, A. C. Barone, R. Bruzzese, V. Iannotti, L. Lanotte, and M. Vitiello, Production of nanoparticles of different materials by means of ultrashort laser pulses, *Appl. Surf. Sci.* **252**, 4678 (2006).
- [12] D. Riabinina, M. Chaker, and J. Margot, Dependence of gold nanoparticle production on pulse duration by laser ablation in liquid media, *Nanotechnology* **23**, 135603 (2012).
- [13] S. Amoruso, R. Bruzzese, X. Wang, N. N. Nedialkov, and P. A. Atanasov, An analysis of the dependence on photon energy of the process of nanoparticle generation by femtosecond laser ablation in a vacuum, *Nanotechnology* **18**, 145612 (2007).
- [14] M. Sanz, M. Walczak, R. de Nalda, M. Oujja, J. F. Marco, J. Rodriguez, J. G. Izquierdo, L. Bañares, and M. Castillejo, Femtosecond pulsed laser deposition of nanostructured TiO₂ films, *Appl. Surf. Sci.* **255**, 5206 (2009).
- [15] S. Noël, J. Hermann, and T. Itina, Investigation of nanoparticle generation during femtosecond laser ablation of metals, *Appl. Surf. Sci.* **253**, 6310 (2007).
- [16] N. Tsakiris, K. K. Anoop, G. Ausanio, M. Gill-Comeau, R. Bruzzese, S. Amoruso, and L. J. Lewis, Ultrashort laser ablation of bulk copper targets: Dynamics and size distribution of the generated nanoparticles, *J. Appl. Phys.* **115**, 243301 (2014).

- [17] S. Eliezer, N. Eliaz, E. Grossman, D. Fisher, I. Gouzman, Z. Henis, S. Pecker, Y. Horovitz, M. Fraenkel, S. Maman, and Y. Lereah, Synthesis of nanoparticles with femtosecond laser pulses, *Phys. Rev. B* **69**, 144119 (2004).
- [18] C. Wu and L. V. Zhigilei, Microscopic mechanisms of laser spallation and ablation of metal targets from large-scale molecular dynamics simulations, *Appl. Phys. A* **114**, 11 (2014).
- [19] S. Amoruso, R. Bruzzese, and X. Wang, Plume composition control in double pulse ultrafast laser ablation of metals, *Appl. Phys. Lett.* **95**, 251501 (2009).
- [20] S. Noël and J. Hermann, Reducing nanoparticles in metal ablation plumes produced by two delayed short laser pulses, *Appl. Phys. Lett.* **94**, 053120 (2009).
- [21] J. Reif, O. Varlamova, M. Bounhalli, M. Muth, and T. Arguirov, Nanostructure formation upon femtosecond ablation from silicon: Effect of double pulses, *Appl. Surf. Sci.* **258**, 9491 (2012).
- [22] J. Schille, L. Schneider, S. Kraft, L. Hartwig, and U. Loeschner, Experimental study on double-pulse laser ablation of steel upon multiple parallel-polarized ultrashort-pulse irradiations, *Appl. Phys. A* **122**, 644 (2016).
- [23] M. Hashida, A. F. Semerok, O. Gobert, G. Petite, Y. Izawa, and J. F. Wagner, Ablation threshold dependence on pulse duration for copper, *Appl. Surf. Sci.* **197–198**, 862 (2002).
- [24] J. Byskov-Nielsen, J.-M. Savolainen, M. S. Christensen, and P. Balling, Ultra-short pulse laser ablation of metals: Threshold fluence, incubation coefficient and ablation rates, *Appl. Phys. A* **101**, 97 (2010).
- [25] J. Byskov-Nielsen, J.-M. Savolainen, M. S. Christensen, and P. Balling, Ultra-short pulse laser ablation of copper, silver and tungsten: Experimental data and two-temperature model simulations, *Appl. Phys. A* **103**, 447 (2011).
- [26] J. P. Colombier, P. Combis, A. Rosenfeld, I. V. Hertel, E. Audouard, and R. Stoian, Optimized energy coupling at ultrafast laser-irradiated metal surfaces by tailoring intensity envelopes: Consequences for material removal from Al samples, *Phys. Rev. B* **74**, 224106 (2006).
- [27] A. De Giacomo, M. Dell’Aglia, D. Bruno, R. Gaudiuso, and O. De Pascale, Experimental and theoretical comparison of single-pulse and double-pulse laser induced breakdown spectroscopy on metallic samples, *Spectrochim. Acta, Part B* **63**, 805 (2008).
- [28] Y. Tian, C. Yan, T. Zhang, H. Tang, H. Li, J. Yu, J. Bernard, L. Chen, S. Martin, N. Delepine-Gilon, J. Bocková, P. Veis, Y. Chen, and J. Yu, Classification of wines according to their production regions with the contained trace elements using laser-induced breakdown spectroscopy, *Spectrochim. Acta, Part B* **135**, 91 (2017).
- [29] J. Bocková, Y. Tian, H. Yin, N. Delepine-Gilon, Y. Chen, P. Veis, and J. Yu, Determination of metal elements in wine using laser-induced breakdown spectroscopy (LIBS), *Appl. Spectrosc.* **71**, 1750 (2017).
- [30] A. Semerok and C. Dutouquet, Ultrashort double pulse laser ablation of metals, *Thin Solid Films* **453–454**, 501 (2004).
- [31] V. Piñon, C. Fotakis, G. Nicolas, and D. Anglos, Double pulse laser-induced breakdown spectroscopy with femtosecond laser pulses, *Spectrochim. Acta, Part B* **63**, 1006 (2008).
- [32] A. A. I. Khalil, Development of double-pulse lasers ablation system for generating gold ion source under applying an electric field, *Opt. Laser Technol.* **75**, 105 (2015).
- [33] X. Zhao and Y. C. Shin, Laser-plasma interaction and plasma enhancement by ultrashort double-pulse ablation, *Appl. Phys. B* **120**, 81 (2015).
- [34] J. Mildner, C. Sarpe, N. Götte, M. Wollenhaupt, and T. Baumert, Emission signal enhancement of laser ablation of metals (aluminum and titanium) by time delayed femtosecond double pulses from femtoseconds to nanoseconds, *Appl. Surf. Sci.* **302**, 291 (2014).
- [35] B. Rethfeld, A. Kaiser, M. Vicanek, and G. Simon, Ultrafast dynamics of nonequilibrium electrons in metals under femtosecond laser irradiation, *Phys. Rev. B* **65**, 214303 (2002).
- [36] D. E. Roberts, A. du Plessis, and L. R. Botha, Femtosecond laser ablation of silver foil with single and double pulses, *Appl. Surf. Sci.* **256**, 1784 (2010).
- [37] X. Zhao and Y. C. Shin, Ablation enhancement of silicon by ultrashort double-pulse laser ablation, *Appl. Phys. Lett.* **105**, 111907 (2014).
- [38] R. Le Harzic, D. Breitling, S. Sommer, C. Föhl, K. König, F. Dausinger, and E. Audouard, Processing of metals by double pulses with short laser pulses, *Appl. Phys. A* **81**, 1121 (2005).
- [39] R. Stoian, M. Boyle, A. Thoss, A. Rosenfeld, G. Korn, I. V. Hertel, and E. E. B. Campbell, Laser ablation of dielectrics with temporally shaped femtosecond pulses, *Appl. Phys. Lett.* **80**, 353 (2002).
- [40] S. Höhm, A. Rosenfeld, J. Krüger, and J. Bonse, Area dependence of femtosecond laser-induced periodic surface structures for varying band gap materials after double pulse excitation, *Appl. Surf. Sci.* **278**, 7 (2013).
- [41] T. J.-Y. Derrien, J. Krüger, T. E. Itina, S. Höhm, A. Rosenfeld, and J. Bonse, Rippled area formed by surface plasmon polaritons upon femtosecond laser double-pulse irradiation of silicon, *Opt. Express* **21**, 29643 (2013).
- [42] T. J.-Y. Derrien, J. Krüger, T. E. Itina, S. Höhm, A. Rosenfeld, and J. Bonse, Rippled area formed by surface plasmon polaritons upon femtosecond laser double-pulse irradiation of silicon: The role of carrier generation and relaxation processes, *Appl. Phys. A* **117**, 77 (2014).
- [43] T. Donnelly, J. G. Lunney, S. Amoruso, R. Bruzzese, X. Wang, and X. Ni, Double pulse ultrafast laser ablation of nickel in vacuum, *J. Appl. Phys.* **106**, 013304 (2009).
- [44] Y. Furukawa, R. Sakata, K. Konishi, K. Ono, S. Matsuoka, K. Watanabe, S. Inoue, M. Hashida, and S. Sakabe, Demonstration of periodic nanostructure formation with less ablation by double-pulse laser irradiation on titanium, *Appl. Phys. Lett.* **108**, 264101 (2016).
- [45] M. E. Povarnitsyn, T. E. Itina, K. V. Khishchenko, and P. R. Levashov, Suppression of Ablation in Femtosecond Double-Pulse Experiments, *Phys. Rev. Lett.* **103**, 195002 (2009).
- [46] M. E. Povarnitsyn, T. E. Itina, P. R. Levashov, and K. V. Khishchenko, Simulation of ultrashort double-pulse laser ablation, *Appl. Surf. Sci.* **257**, 5168 (2011).
- [47] V. B. Fokin, M. E. Povarnitsyn, and P. R. Levashov, Simulation of ablation and plume dynamics under femtosecond double-pulse laser irradiation of aluminum: Comparison of atomistic and continual approaches, *Appl. Surf. Sci.* **396**, 1802 (2017).
- [48] J. Roth, A. Krauß, J. Lotze, and H.-R. Trebin, Simulation of laser ablation in aluminum: The effectivity of double pulses, *Appl. Phys. A* **117**, 2207 (2014).

- [49] M. E. Povarnitsyn, V. B. Fokin, P. R. Levashov, and T. E. Itina, Molecular dynamics simulation of subpicosecond double-pulse laser ablation of metals, *Phys. Rev. B* **92**, 174104 (2015).
- [50] C.-W. Cheng and J.-K. Chen, Drilling of copper using a dual-pulse femtosecond laser, *Technologies* **4**, 7 (2016).
- [51] C. M. Liebig, P. Srisungsitthisunti, A. M. Weiner, and X. Xu, Enhanced machining of steel using femtosecond pulse pairs, *Appl. Phys. A* **101**, 487 (2010).
- [52] Y. Rosandi and H. M. Urbassek, Ultrashort-pulse laser irradiation of metal films: The effect of a double-peak laser pulse, *Appl. Phys. A* **101**, 509 (2010).
- [53] S. Amoruso, R. Bruzzese, X. Wang, G. O'Connell, and J. G. Lunney, Multidiagnostic analysis of ultrafast laser ablation of metals with pulse pair irradiation, *J. Appl. Phys.* **108**, 113302 (2010).
- [54] Q. Wang, S. Luo, Z. Chen, H. Qi, J. Deng, and Z. Hu, Drilling of aluminum and copper films with femtosecond double-pulse laser, *Opt. Laser Technol.* **80**, 116 (2016).
- [55] V. I. Babushok, F. C. DeLucia Jr., J. L. Gottfried, C. A. Munson, and A. W. Miziolek, Double pulse laser ablation and plasma: Laser induced breakdown spectroscopy signal enhancement, *Spectrochim. Acta, Part B* **61**, 999 (2006).
- [56] E. Axente, I. N. Mihailescu, J. Hermann, and T. E. Itina, Probing electron-phonon coupling in metals via observations of ablation plumes produced by two delayed short laser pulses, *Appl. Phys. Lett.* **99**, 081502 (2011).
- [57] D. Perez and L. J. Lewis, Ablation of Solids under Femtosecond Laser Pulses, *Phys. Rev. Lett.* **89**, 255504 (2002).
- [58] P. Lorazo, L. J. Lewis, and M. Meunier, Thermodynamic pathways to melting, ablation, and solidification in absorbing solids under pulsed laser irradiation, *Phys. Rev. B* **73**, 134108 (2006).
- [59] S. Amoruso, R. Bruzzese, X. Wang, and J. Xia, Ultrafast laser ablation of metals with a pair of collinear laser pulses, *Appl. Phys. Lett.* **93**, 191504 (2008).
- [60] M. Gill-Comeau and L. J. Lewis, Ultrashort-pulse laser ablation of nanocrystalline aluminum, *Phys. Rev. B* **84**, 224110 (2011).
- [61] S. I. Ashitkov, N. A. Inogamov, V. V. Zhakhovskii, Y. N. Emirov, M. B. Agranat, I. I. Oleinik, S. I. Anisimov, and V. E. Fortov, Formation of nanocavities in the surface layer of an aluminum target irradiated by a femtosecond laser pulse, *JETP Lett.* **95**, 176 (2012).
- [62] E. I. Ageev, V. Y. Bychenkov, V. P. Veiko, A. A. Ionin, S. I. Kudryashov, A. A. Petrov, and A. A. Samokhvalov, Double-pulse femtosecond laser ablation of the surface of stainless steel with variable interpulse delays, *JETP Lett.* **104**, 421 (2016).
- [63] R. R. Zope and Y. Mishin, Interatomic potentials for atomistic simulations of the Ti-Al system, *Phys. Rev. B* **68**, 024102 (2003).
- [64] Z. Lin, L. V. Zhigilei, and V. Celli, Electron-phonon coupling and electron heat capacity of metals under conditions of strong electron-phonon nonequilibrium, *Phys. Rev. B* **77**, 075133 (2008).
- [65] B. H. Christensen, K. Vestentoft, and P. Balling, Short-pulse ablation rates and the two-temperature model, *Appl. Surf. Sci.* **253**, 6347 (2007).
- [66] D. S. Ivanov and L. V. Zhigilei, Combined atomistic-continuum modeling of short-pulse laser melting and disintegration of metal films, *Phys. Rev. B* **68**, 064114 (2003).
- [67] C. Schäfer, H. M. Urbassek, L. V. Zhigilei, and B. J. Garrison, Pressure-transmitting boundary conditions for molecular-dynamics simulations, *Comput. Mater. Sci.* **24**, 421 (2002).
- [68] S. I. Anisimov, B. L. Kapeliovich, and T. L. Perel'man, Electron emission from metal surfaces exposed to ultrashort laser pulses, *Sov. Phys.-JETP* **39**, 375 (1974).
- [69] C. L. Kelchner, S. J. Plimpton, and J. C. Hamilton, Dislocation nucleation and defect structure during surface indentation, *Phys. Rev. B* **58**, 11085 (1998).
- [70] M. E. Povarnitsyn, N. E. Andreev, E. M. Apfelbaum, T. E. Itina, K. V. Khishchenko, O. F. Kostenko, P. R. Levashov, and M. E. Veysman, A wide-range model for simulation of pump-probe experiments with metals, *Appl. Surf. Sci.* **258**, 9480 (2012).
- [71] A. Stukowski, Visualization and analysis of atomistic simulation data with OVITO—the Open Visualization Tool, *Modell. Simul. Mater. Sci. Eng.* **18**, 015012 (2010).
- [72] See Supplemental Material at <http://link.aps.org/supplemental/10.1103/PhysRevB.97.224301> for “animation.avi” showing the time evolution of the atomic positions for all the simulations reported in this work.
- [73] See Supplemental Material at <http://link.aps.org/supplemental/10.1103/PhysRevB.97.224301> for “animation2.avi” showing the subsurface voids in the case of all the simulations reported in this work.
- [74] R. L. Webb, J. T. Dickinson, and G. J. Exarhos, Characterization of particulates accompanying laser ablation of NaNO_3 , *Appl. Spectrosc.* **51**, 707 (1997).
- [75] L. V. Zhigilei and B. J. Garrison, Mechanisms of laser ablation from molecular dynamics simulations: Dependence on the initial temperature and pulse duration, *Appl. Phys. A* **69**, S75 (1999).
- [76] S. Noël, E. Axente, and J. Hermann, Investigation of plumes produced by material ablation with two time-delayed femtosecond laser pulses, *Appl. Surf. Sci.* **255**, 9738 (2009).
- [77] S. Singha, Z. Hu, and R. J. Gordon, Ablation and plasma emission produced by dual femtosecond laser pulses, *J. Appl. Phys.* **104**, 113520 (2008).
- [78] X. Li, L. Jiang, and H.-L. Tsai, Phase change mechanisms during femtosecond laser pulse train ablation of nickel thin films, *J. Appl. Phys.* **106**, 064906 (2009).
- [79] G. Yang, *Laser Ablation in Liquids: Principles and Applications in the Preparation of Nanomaterials* (Pan Stanford Publishing, Singapore, 2012).
- [80] M. Blander and J. L. Katz, Bubble nucleation in liquids, *AIChE J.* **21**, 833 (1975).
- [81] A. Stukowski, Computational analysis methods in atomistic modeling of crystals, *JOM* **66**, 399 (2014).
- [82] C. Kerse, H. Kalaycioglu, P. Elahi, B. Cetin, D. K. Kesim, O. Akcaalan, S. Yavas, M. D. Asik, B. Oktem, H. Hoogland, R. Holzwarth, and F. O. Ilday, Ablation-cooled material removal with ultrafast bursts of pulses, *Nature (London)* **537**, 84 (2016).
- [83] P. R. Herman, A. Oettl, K. P. Chen, and R. S. Marjoribanks, Laser micromachining of transparent fused silica with 1-ps pulses and pulse trains, *Proc. SPIE* **3616**, 148 (1999).
- [84] Z. Han, C. Zhou, E. Dai, and J. Xie, Ultrafast double pulses ablation of Cr film on glass, *Opt. Commun.* **281**, 4723 (2008).
- [85] J. Scaffidi, S. M. Angel, and D. A. Cremers, Emission enhancement mechanisms in dual-pulse LIBS, *Anal. Chem.* **78**, 24 (2006).

- [86] R. Glaus and D. W. Hahn, Double-pulse laser ablation coupled to laser-induced breakdown spectroscopy, *Spectrochim. Acta, Part B* **98**, 48 (2014).
- [87] I. Lopez-Quintas, V. Lorient, D. Avila, J. G. Izquierdo, E. Rebollar, L. Banares, M. Castillejo, R. de Nalda, and M. Martin, Ablation dynamics of Co/ZnS targets under double pulse femtosecond laser irradiation, *Phys. Chem. Chem. Phys.* **18**, 3522 (2016).
- [88] Y. Qi, H. Qi, Q. Wang, Z. Chen, and Z. Hu, The influence of double pulse delay and ambient pressure on femtosecond laser ablation of silicon, *Opt. Laser Technol.* **66**, 68 (2015).
- [89] M. G. Martin, MCCCSTowhee: A tool for Monte Carlo molecular simulation, *Mol. Simul.* **39**, 1212 (2013).
- [90] Z. Insepov, T. Bazhirov, G. E. Norman, and V. V. Stegailov, *Joint International Topical Meeting on Mathematics & Computation and Supercomputing in Nuclear Applications (M&C + SNA 2007) Monterey, California, April 15-19, 2007, on CD-ROM* (American Nuclear Society, LaGrange Park, IL, 2007).
- [91] V. Morel, A. Bultel, and B. G. Chéron, The critical temperature of aluminum, *Int. J. Thermophys.* **30**, 1853 (2009).
- [92] J. Alexandre, D. J. Tildesley, and G. A. Chapela, Molecular dynamics simulation of the orthobaric densities and surface tension of water, *J. Chem. Phys.* **102**, 4574 (1995).
- [93] M. Leitner, T. Leitner, A. Schmon, K. Aziz, and G. Pottlacher, Thermophysical properties of liquid aluminum, *Metall. Mater. Trans. A* **48**, 3036 (2017).
- [94] J. M. Molina, R. Voytovych, E. Louis, and N. Eustathopoulos, The surface tension of liquid aluminium in high vacuum: The role of surface condition, *Int. J. Adhes. Adhes.* **27**, 394 (2007).
- [95] H. Kobatake, J. Brillo, J. Schmitz, and P.-Y. Pichon, Surface tension of binary Al-Si liquid alloys, *J. Mater. Sci.* **50**, 3351 (2015).